

2022

Catalytic Thermal Decomposition of NO₂ by Iron(III) Nitrate Nonahydrate-Doped Poly(Vinylidene Difluoride)

Lasanthi Sumathirathne

University of Rhode Island

Carson Lawrence Hasselbrink

University of Rhode Island

Dugan Hayes

University of Rhode Island, dugan@uri.edu

William B. Euler

University of Rhode Island, billeuler@uri.edu

Follow this and additional works at: https://digitalcommons.uri.edu/chm_facpubs

Citation/Publisher Attribution

Sumathirathne, L., Hasselbrink, C. L., Hayes, D., & Euler, W. B. (2022). Catalytic Thermal Decomposition of NO₂ by Iron(III) Nitrate Nonahydrate-Doped Poly(Vinylidene Difluoride). *ACS Omega*, 7(48), 43839-43846.

<https://doi.org/10.1021/acsomega.2c04970>

Available at: <https://doi.org/10.1021/acsomega.2c04970>

Catalytic Thermal Decomposition of NO₂ by Iron(III) Nitrate Nonahydrate-Doped Poly(Vinylidene Difluoride)

Creative Commons License



This work is licensed under a [Creative Commons Attribution-Noncommercial-No Derivative Works 4.0 License](#).

Creative Commons License



This work is licensed under a [Creative Commons Attribution-Noncommercial-No Derivative Works 4.0 License](#).

Catalytic Thermal Decomposition of NO₂ by Iron(III) Nitrate Nonahydrate-Doped Poly(Vinylidene Difluoride)

Lasanthi Sumathirathne, Carson Lawrence Hasselbrink, Dugan Hayes, and William B. Euler*



Cite This: ACS Omega 2022, 7, 43839–43846



Read Online

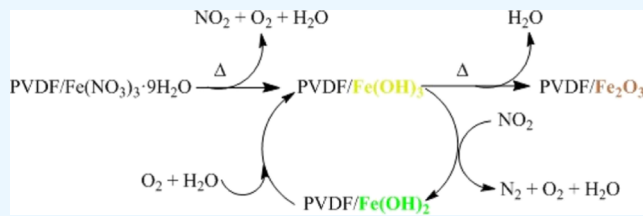
ACCESS |

Metrics & More

Article Recommendations

Supporting Information

ABSTRACT: The products of thermal decomposition of iron nitrate nonahydrate doped into poly(vinylidene difluoride) are examined using Mössbauer spectroscopy. Very little of the expected nitrogen dioxide product is observed, which is attributed to Fe³⁺ catalysis of the decomposition of NO₂. The active site of the catalysis is shown to be Fe(OH)₃ in the polymer matrix, which is, unexpectedly, reduced to Fe(OH)₂. Thermodynamic calculations show that the reduction of Fe³⁺ is exergonic at sufficiently high temperatures. A reaction sequence, including a catalytic cycle for decomposition of NO₂, is proposed that accounts for the observed reaction products. The role of the polymer matrix is proposed to inhibit transport of gas-phase products, which allows them to interact with Fe(OH)₃ doped in the polymer.



INTRODUCTION

Poly(vinylidene difluoride) (PVDF) has been studied for several decades because it has unique electrical properties.^{1–14} PVDF is primarily found in three phases (although other minor phases have been reported). In the α -phase, the polymer is nonpolar and chemically inert, so it has found use as a plastic support in chemically aggressive environments. The β -phase is the most electroactive being ferroelectric, piezoelectric, and pyroelectric. The γ -phase is piezoelectric and pyroelectric but does not support a permanent electric moment. The α -phase is easily fabricated by deposition from low-polarity solvents or melt-casting.^{3,7,15} The β -phase is the most difficult to obtain and is typically fabricated by electric field poling, that is, cooling a stretched sample under the influence of an electric field.¹² More recently, tuning of the phase behavior and properties of PVDF has been accomplished by doping with nanoparticles or metal-ion salts.^{7,16–31} All of these efforts to exploit various properties of PVDF are under continuous study to find improved sensors,^{29,32,33} modified optical properties,^{18,34,35} lithium-ion battery membranes,^{36–38} energy-harvesting devices,^{11,39–43} electromagnetic shielding materials,^{26,28} catalysts,^{22,24,30,44–48} computer memory,^{10,49,50} or antifouling membranes.⁵¹

The catalytic effect of PVDF on the thermal decomposition of transition-metal nitrate hydrates doped into the polymer was recently described.⁴⁸ When the transition-metal ion carried a 2+ charge, the surrounding PVDF matrix catalyzed the reaction of the nitrate ion into gas-phase nitrogen oxides, solid-phase binary metal oxides, and other products, lowering the decomposition temperature by over 100 °C in some cases. In contrast, for trivalent transition-metal ions, there was little evidence of catalysis, which was attributed to the slow ion migration required to form the multiatom metal oxides.

Moreover, with the trivalent metal ions, the generation of gas-phase nitrogen oxides was suppressed, with gas-phase IR signals at noise levels. It was hypothesized that the decomposition of NO_x was catalyzed by the 3 + transition-metal oxides, in accordance with literature precedence.^{52–54} There has been a continuing interest for many years in finding new catalysts to remove NO_x gases,^{55–60} so confirmation of this hypothesis is of great significance.

In this report, we use Mössbauer spectroscopy to better understand the compositional changes that occur during the thermal decomposition of Fe(NO₃)₃·9H₂O doped into PVDF. Similar to previous studies,⁶¹ it is determined that iron hydroxides are intermediates prior to the final formation of Fe₂O₃ in the PVDF matrix. Further, it is these hydroxides that are responsible for the removal of NO₂, not the final oxide. Thermodynamic calculations demonstrate that the reduction of Fe(OH)₃ to Fe(OH)₂ concurrent with NO₂ decomposition to N₂ and O₂ is exergonic. In competition with the Fe³⁺ reduction, the generated O₂ can oxidize Fe²⁺ back to Fe³⁺, so that the final product is always Fe₂O₃. Identification of the hydroxides as critical to the NO_x decomposition may help develop better catalysts for removal of these gases.

Received: August 4, 2022

Accepted: November 7, 2022

Published: November 17, 2022



■ EXPERIMENTAL SECTION

PVDF ($M_w \sim 534,000 \text{ g}\cdot\text{mol}^{-1}$) and $\text{Fe}(\text{NO}_3)_3\cdot 9\text{H}_2\text{O}$ were purchased from Sigma-Aldrich, and acetone and N,N -dimethylformamide (DMF) were purchased from Fisher Scientific. Thin-film samples were fabricated on precleaned glass substrates using a dip coating method. For that, 10% (w/v) PVDF solutions were prepared using a solvent composed of a mixture of 9:1 (v/v) acetone: DMF. This solution was sonicated in a water bath for 3 h at 40 °C. The amount of $\text{Fe}(\text{NO}_3)_3\cdot 9\text{H}_2\text{O}$ required to form 4 mol % of Fe^{3+} in PVDF (relative to the repeat units) was added to the prepared PVDF solution and sonicated for another 2 min without heat.

Thin films were formed using an MTI dip-coater (model TL0.01) under an N_2 environment to control the humidity and at a withdrawal rate of 124 $\text{mm}\cdot\text{min}^{-1}$. The prepared samples were annealed 2 min in an oven at 60 °C to evaporate the excess solvent. The samples were peeled off the substrate and cut to $2.5 \times 2.5 \text{ cm}$ dimension. Then, ~40 thin films were packed in an aluminum pan to give a high enough quantity of ^{57}Fe for spectroscopic analysis in the natural abundance samples. The composite samples were about 20 μm thick and contained about 17 μg of ^{57}Fe . These samples were heated to critical temperatures using a furnace (MTI Corporation EQ-CVF-1300T) with a $5 \text{ }^{\circ}\text{C}\cdot\text{min}^{-1}$ rate under an N_2 atmosphere. The heated samples were immediately cooled down to room temperature by removing them from the oven. Another set of samples were prepared in the same fashion with 5 h annealing time at the chosen temperature.

The characterization of $\text{Fe}^{3+}/\text{PVDF}$ thin films and pure $\text{Fe}(\text{NO}_3)_3\cdot 9\text{H}_2\text{O}$ samples were carried out using a Mössbauer spectrometer (SEE Co. Resonant Gamma-Ray Spectrometer model W304) with a ^{57}Co source at room temperature. Metallic α -Fe foil (30 μm) was used as a reference for calibration of the velocity scale. The velocity window $\pm 4 \text{ mm}\cdot\text{s}^{-1}$ was selected for the thin-film samples as it fully captured all transmittance peaks. Mössbauer spectra of the pure salt at selected temperatures were also collected for comparison. Spectral parameters were obtained by fitting data using the MossA 1.01g software package⁶² to give isomer shifts (δ), full width at half-maxima (Γ), and quadrupole splittings (ΔE_Q). All XRD data were measured using a Rigaku-Miniflex 600 diffractometer using a Cu $\text{K}\alpha$ source with 0.154 nm wavelength, an accelerating voltage of 40 KV, and a tube current of 15 mA. A Perkin-Elmer Spectrum 100 infrared spectrometer in the attenuated total reflectance mode was used to collect vibrational spectra with a 4 cm^{-1} resolution. Scanning electron microscopy (SEM) images were obtained using a Zeiss Sigma VP field emission scanning electron microscope in the backscatter mode with an Oxford Instruments X-max 50 mm^2 energy dispersive X-ray spectroscopy (EDS/EDX) detector.

■ RESULTS AND DISCUSSION

$\text{Fe}^{3+}/\text{PVDF}$ composite thin films were fabricated by doping PVDF with $\text{Fe}(\text{NO}_3)_3\cdot 9\text{H}_2\text{O}$ in solution and casting the films using dip coating. The prepared room-temperature thin films were yellow in color indicating a weak ligand coordination sphere around the Fe^{3+} in the thin films. The IR data of the fabricated thin films⁴⁸ (Figure S1) kept at 25 °C show peaks related to C–H stretching at $\sim 3000 \text{ cm}^{-1}$ and the presence of residual solvents including H_2O (OH stretching at $\sim 3400 \text{ cm}^{-1}$) and DMF (C=O stretching at 1660 cm^{-1}). Further,

these thin films are primarily in the polar β -phase with a trace amount of nonpolar α -phase as indicated by the intense peak at 1275 cm^{-1} (β -phase marker) and 840 cm^{-1} (a combination peak of β - and γ -phases) and a less intense peak at 764 cm^{-1} (α -phase marker).^{3,9,63} The charge from the Fe^{3+} dopant aligns the bond dipole moments of the polymer chain to give a β -phase crystalline fraction as high as 0.69, as calculated using Beer's law with the peaks at 840 and 764 cm^{-1} from the IR data.⁶³ Further, the XRD data from these films are consistent with the FTIR data, showing a high fraction of polar phases in thin-film samples kept at room temperature.⁴⁸ The XRD data does not have any peaks related to the initial crystalline iron salt, indicating that the dopants are fully dissolved in the composite thin films.⁴⁸

To further demonstrate that the iron ions are uniformly distributed, SEM/EDS measurements were made, as shown in Figure 1. The SEM image shows that the PVDF film is

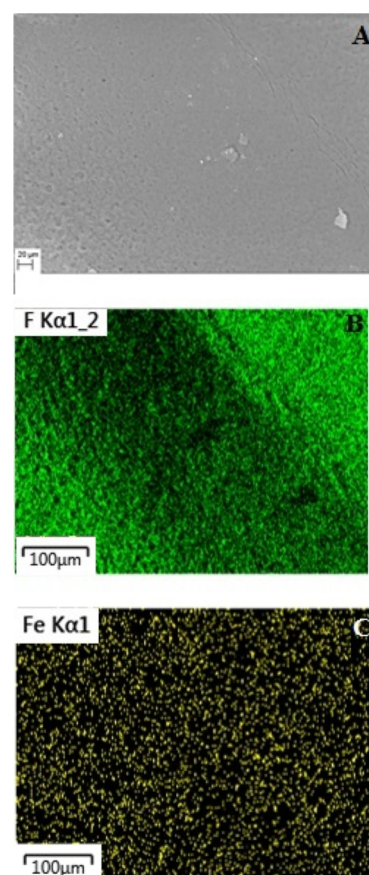


Figure 1. A) SEM image of a PVDF film doped with $\text{Fe}(\text{NO}_3)_3\cdot 9\text{H}_2\text{O}$. (B) F elemental distribution (green). (C) Fe^{3+} distribution (yellow).

generally smooth with an unremarkable surface morphology. The elemental analysis found from the EDS measurement shows that the surface is primarily dominated by F atoms, while the Fe^{3+} ions are located throughout the entire sample area. There is no evidence of aggregation of iron ions. Integration of the F and Fe^{3+} signals shows that the Fe/F mole ratio is 0.021 or 0.042 Fe^{3+} ions per polymer repeat unit, consistent with the preparation conditions.

$\text{Fe}(\text{NO}_3)_3\cdot 9\text{H}_2\text{O}$ decomposes thermally to give NO_2 , H_2O , and Fe_2O_3 .⁴⁸ The Mössbauer spectra of $\text{Fe}(\text{NO}_3)_3\cdot 9\text{H}_2\text{O}$

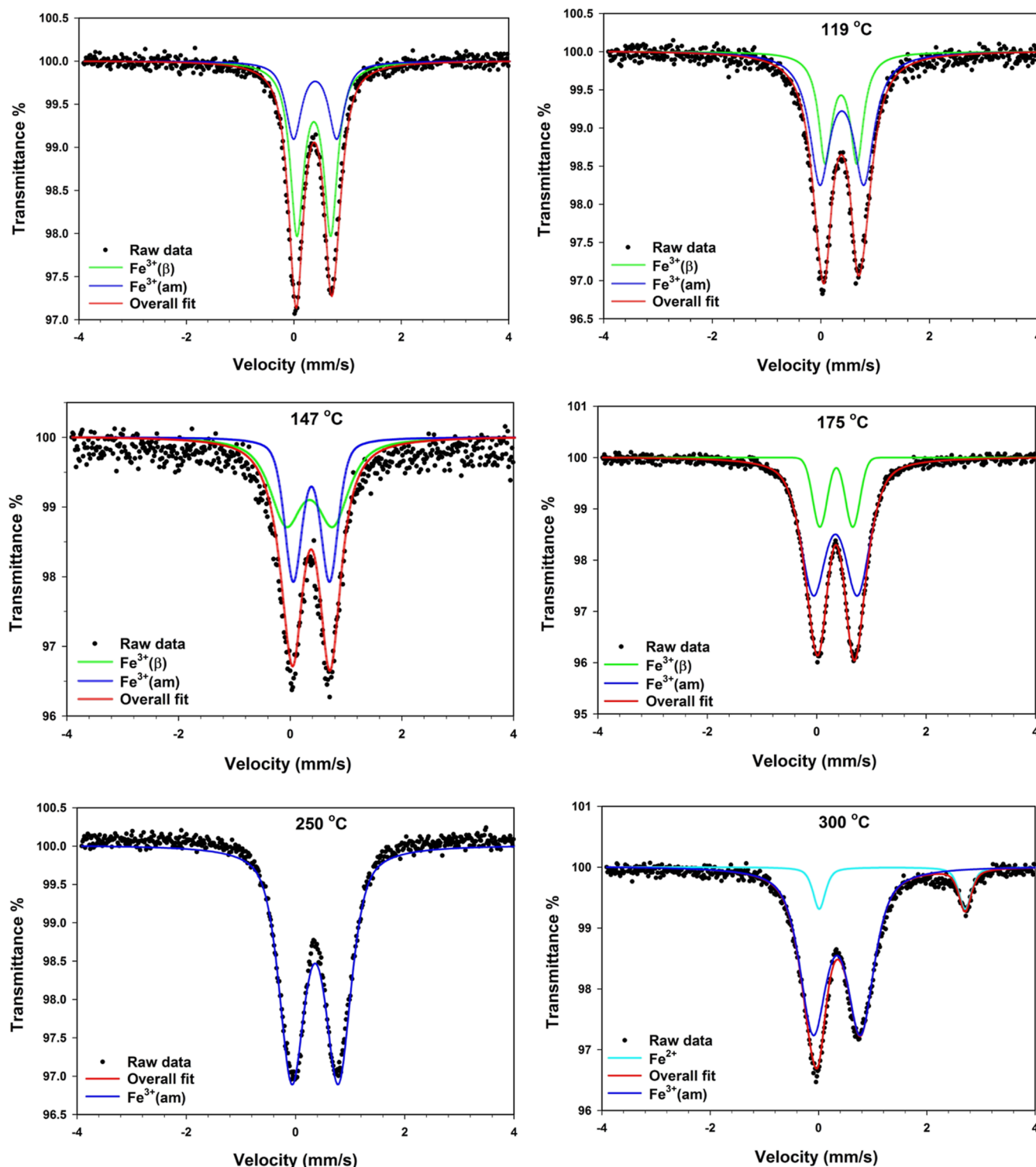


Figure 2. Mössbauer spectra of Fe^{3+} /PVDF thin films heated to the indicated temperature and then quenched to room temperature. The measured data are shown as closed circles, the total fits to the data are red lines, and the components to the total fits are blue, green, or cyan lines.

heated to several temperatures are shown in Figure S2. At room temperature, the spectrum can be fitted with two components: a broad peak with isomer shift $\delta_1 = 0.44 \pm 0.04 \text{ mm}\cdot\text{s}^{-1}$ (line width $4.27 \text{ mm}\cdot\text{s}^{-1}$) and a narrow peak with isomer shift $\delta_2 = 0.34 \pm 0.01 \text{ mm}\cdot\text{s}^{-1}$ (line width $0.95 \text{ mm}\cdot\text{s}^{-1}$). Any quadrupole splitting that may be present is not resolved. The isomer shifts are consistent with Fe^{3+} , and the small quadrupole coupling is consistent with an octahedral

coordination in a symmetric (${}^6\text{A}_{1g}$) high-spin ($t_{2g}^3 e_g^2$) electronic state. The electric field gradient from the Fe^{3+} electronic state and octahedral coordination is 0, and the contribution from the surrounding environment would be small. Figure S3 shows the powder X-ray diffractogram of $\text{Fe}(\text{NO}_3)_3 \cdot 9\text{H}_2\text{O}$, which is consistent with a monoclinic crystal structure. Upon heating to 250 or 300 °C, thermal decomposition of the salt occurs, as shown in Figure S2.

When the thermal products are quenched, the Mössbauer spectra again show two Fe^{3+} sites at (250 °C: $\delta_1 = 0.326 \pm 0.004 \text{ mm}\cdot\text{s}^{-1}$, $\Delta E_{Q1} = 0.89 \pm 0.08 \text{ mm}\cdot\text{s}^{-1}$, $\delta_2 = 0.346 \pm 0.007 \text{ mm}\cdot\text{s}^{-1}$, $\Delta E_{Q2} = 0.54 \pm 0.03 \text{ mm}\cdot\text{s}^{-1}$, 300 °C: $\delta_1 = 0.330 \pm 0.002 \text{ mm}\cdot\text{s}^{-1}$, $\Delta E_{Q1} = 0.87 \pm 0.02 \text{ mm}\cdot\text{s}^{-1}$, $\delta_2 = 0.357 \pm 0.003 \text{ mm}\cdot\text{s}^{-1}$, $\Delta E_{Q2} = 0.55 \pm 0.01 \text{ mm}\cdot\text{s}^{-1}$). These are consistent with Fe(OH)_3 or FeOOH as previously reported,^{62–64} although in an amorphous environment rather than crystalline. When the thermal products are annealed for 5 h, a third component is formed that is identified as crystalline Fe_2O_3 (250 °C: $\delta = 0.32 \pm 0.02 \text{ mm}\cdot\text{s}^{-1}$, $\Delta E_Q = 0$, hyperfine splitting = $50.3 \pm 0.1 \text{ mm}\cdot\text{s}^{-1}$, 300 °C: $\delta_1 = 0.34 \pm 0.01 \text{ mm}\cdot\text{s}^{-1}$, $\Delta E_Q = 0$, hyperfine splitting = $50.6 \pm 0.1 \text{ mm}\cdot\text{s}^{-1}$).⁶⁴ The XRD data (Figure S3) show that the samples heated to 250 or 300 °C but not annealed are largely amorphous, but annealing leads to formation of crystalline Fe_2O_3 , consistent with the Mössbauer spectra.⁶⁴

When the Fe^{3+} -doped PVDF films were heated, the only changes in the IR spectra noted (Figure S1) were loss of residual solvent and conversion of the PVDF crystallinity from primarily β -phase to primarily α -phase. The solvent loss was mostly complete when the films were heated to 175 °C, although there were small peaks associated with OH groups up to 300 °C. The formation of α -phase PVDF only occurred when the films were heated above the melting point of β -phase PVDF (which was about 147 °C for these doped PVDF films, slightly depressed from 160 °C for pure β -PVDF⁷). XRD shows similar behavior.⁴⁸ Neither technique provides insight into the changes in the iron ion dopant. However, as previously reported, the gas-phase products show no evidence of NO_2 , indicating a different thermal decomposition pathway when $\text{Fe(NO}_3)_3\cdot9\text{H}_2\text{O}$ is doped in PVDF.

The Mössbauer spectra of $\text{Fe}^{3+}/\text{PVDF}$ thin films heated to selected temperatures and then quenched to room temperature are shown in Figure 2 (wider velocity range spectra were measured to look for other peaks, but none were found). The spectrum of the sample kept at room temperature is an asymmetric doublet with a narrow line width, indicating the iron ions are likely isolated but occupy two slightly different microenvironments. Deconvolution of the spectrum gives $\delta_1 = 0.38 \pm 0.02 \text{ mm}\cdot\text{s}^{-1}$, $\Gamma_1 = 0.35 \pm 0.08 \text{ mm}\cdot\text{s}^{-1}$, $\Delta E_{Q1} = 0.8 \pm 0.2 \text{ mm}\cdot\text{s}^{-1}$ and $\delta_2 = 0.36 \pm 0.01 \text{ mm}\cdot\text{s}^{-1}$, $\Gamma_2 = 0.30 \pm 0.03 \text{ mm}\cdot\text{s}^{-1}$, $\Delta E_{Q2} = 0.63 \pm 0.03 \text{ mm}\cdot\text{s}^{-1}$. The isomer shifts are consistent with Fe^{3+} ,^{65–67} as expected from the fabrication conditions. The larger quadrupole coupling for site 1 is assigned to Fe^{3+} located in amorphous regions, and site 2 is assigned to Fe^{3+} located in β -phase regions of the thin film. Since the α -phase is nonpolar, the electric field gradient is expected to be small with a near-zero quadrupole coupling. When the thin films are heated to temperatures below the PVDF melting point, there are small changes in the Mössbauer spectra indicative of some mobility of Fe^{3+} ions between the different environments. However, when the PVDF melts and then is recooled, the β -phase is lost, and the resulting Mössbauer spectra only show features associated with site 1: $\delta \sim 0.35 \text{ mm}\cdot\text{s}^{-1}$ and $\Delta E_Q \sim 0.85 \text{ mm}\cdot\text{s}^{-1}$. The fit parameters for the Fe^{3+} species as a function of temperature are shown in Figure 2. The values found for the Fe^{3+} isomer shifts and quadrupole couplings found after heating the PVDF-doped composites to temperatures above 175 °C are consistent with the formation of Fe(OH)_3 or FeOOH , as with the decomposition of the pure material. This assignment is supported by the IR spectra (Figure S1) as well, where there are small absorbance features in the OH stretching region of

the spectra of the heated materials at temperatures far above those at which the C=O band from the residual DMF has disappeared. However, the intermediate hydroxides are located in the amorphous or α -phase regions of the PVDF upon cooling. The α -phase is nonpolar, and the amorphous regions are expected to have low polarity as well, so the electronic microenvironments surrounding the Fe^{3+} are similar throughout the entire polymer film, leading to δ and ΔE_Q values similar to the room-temperature spectra. As shown in Figure 3,

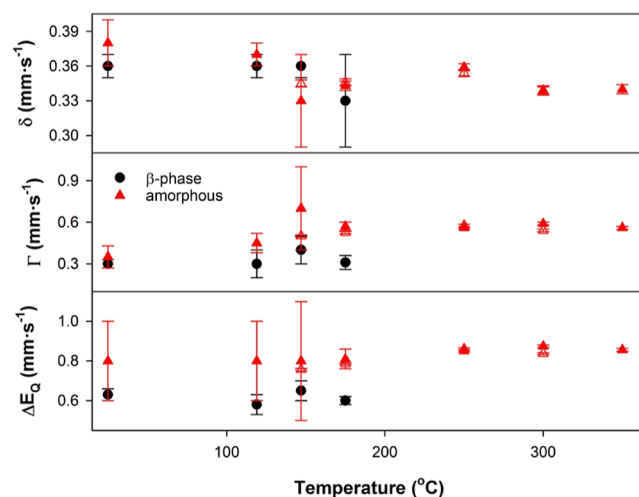
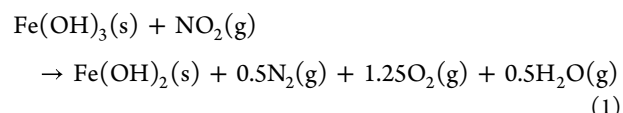


Figure 3. Isomer shifts, δ (top), full width at half-maxima, Γ (middle), and quadrupole couplings, ΔE_Q (bottom), of the Fe^{3+} sites as a function of temperature. Black circles are assigned to sites in the β -phase region of PVDF, and red triangles are assigned to sites in the amorphous regions of the polymer.

the biggest effect of the PVDF environment on the Mössbauer spectrum is the reduction of the quadrupole splitting for Fe^{3+} ions located in β -phase regions. Since the β -phase is expected to have a large constant local electric field, it makes sense that the electric field gradient, which determines the magnitude of the quadrupole coupling, around the Fe^{3+} will be reduced.

When the films are heated to 300 °C, a new peak is found at $\sim 3.2 \text{ mm}\cdot\text{s}^{-1}$. Deconvolution of the high-temperature spectrum shows that the new peak has $\delta = 1.359 \pm 0.009 \text{ mm}\cdot\text{s}^{-1}$, $\Gamma = 0.28 \pm 0.02 \text{ mm}\cdot\text{s}^{-1}$, and $\Delta E_Q = 2.69 \pm 0.02 \text{ mm}\cdot\text{s}^{-1}$, which are assigned to Fe(OH)_2 .⁶⁵ To investigate the origin of the Fe(OH)_2 component, the time dependence of the thermal reaction was measured at 250 °C and 300 °C, as shown in Figure 4. At 250 °C, the feature at $2.7 \text{ mm}\cdot\text{s}^{-1}$ grows with annealing time, indicating no Fe(OH)_2 initially to a significant peak after 2 h. In contrast, at 300 °C, the Fe(OH)_2 content is present when the sample is immediately quenched and then generally diminishes with annealing.

The observations can be explained by the reduction of Fe(OH)_3 by NO_2



This reaction becomes exergonic for temperatures greater than 271 °C (calculated using the Shomate equation and data from the NIST Chemistry web book⁶⁸). This reaction accounts for the absence of NO_2 in the gas-phase IR spectra reported

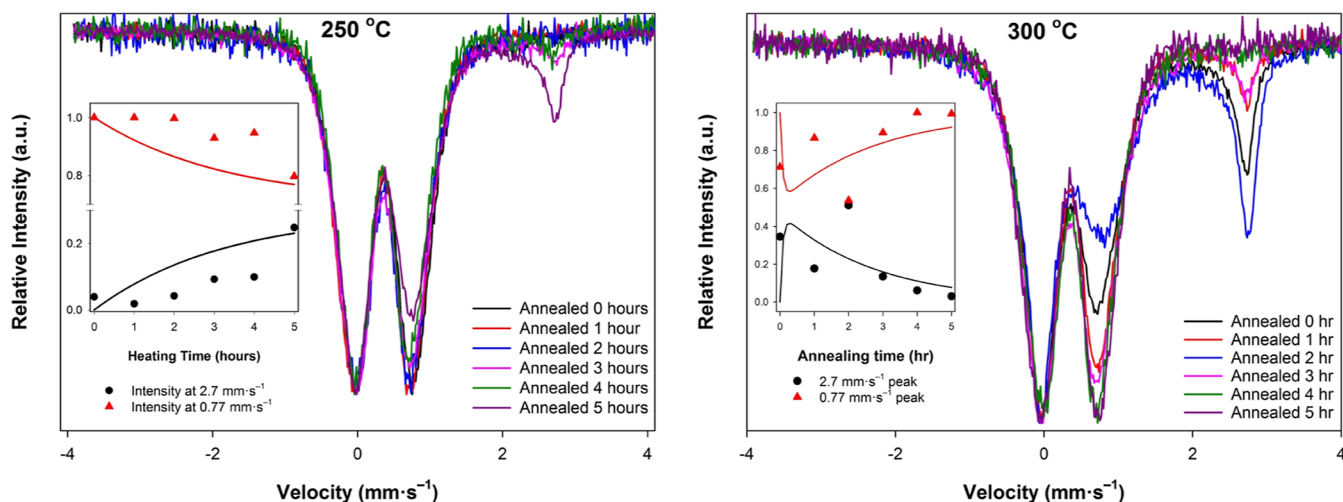
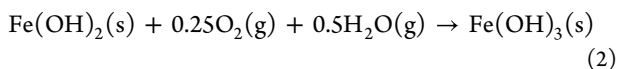


Figure 4. Temporal evolution of the Mössbauer spectra of Fe^{3+} /PVDF samples at $250\text{ }^{\circ}\text{C}$ and $300\text{ }^{\circ}\text{C}$. The spectra are normalized to the peak near $0\text{ mm}\cdot\text{s}^{-1}$. The insets show the intensities of the peaks at $2.7\text{ mm}\cdot\text{s}^{-1}$ (black circles) and $0.77\text{ mm}\cdot\text{s}^{-1}$ (red triangles). The lines are modeled using the kinetic equations discussed in the text.

earlier.⁴⁸ The reoxidation of Fe(OH)_2 by dioxygen is exergonic throughout the entire temperature range investigated



The temperature dependence of ΔG° for eqs 1 and 2 are shown in Figure 5. Reaction (1) becomes more favorable as

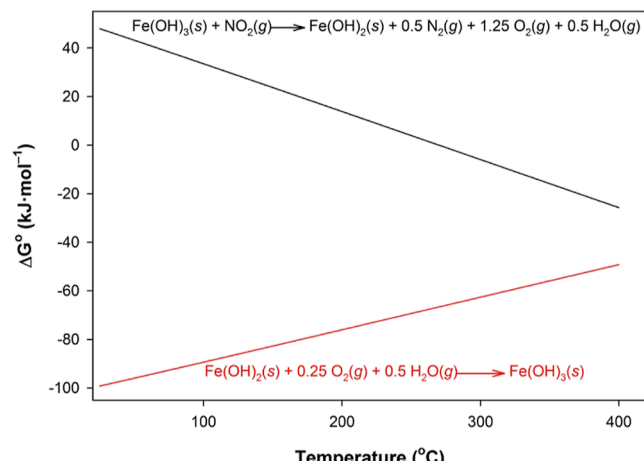


Figure 5. ΔG° calculated for the indicated reactions using the Shomate equation.

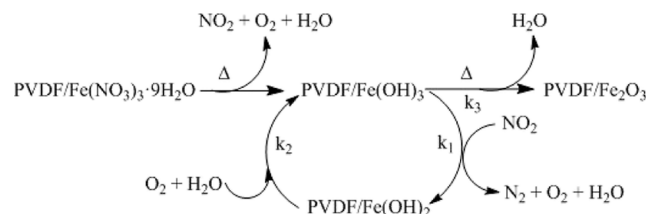
the temperature increases. At $250\text{ }^{\circ}\text{C}$, the reduction of the Fe^{3+} species is slightly endergonic. The reoxidation of Fe(OH)_2 is thermodynamically very favorable, but access to other gas-phase reactants, O_2 and H_2O , is limited in the thin films, so that the reduced iron can remain stable for several hours.

Scheme 1 summarizes the thermal reactions of the $\text{Fe}(\text{NO}_3)_3\cdot 9\text{H}_2\text{O}$ -doped PVDF thin films. The rate equations for the catalytic cycle are given in the Supporting Information and can be solved by linearizing the rate constants as

$$k'_1 = k_1[\text{NO}_2] + k_3 \quad (3)$$

$$k'_2 = k_2[\text{O}_2]^{1/4}[\text{H}_2\text{O}]^{1/2} \quad (4)$$

Scheme 1. Reaction Sequence in the Thermal Decomposition of $\text{Fe}(\text{NO}_3)_3\cdot 9\text{H}_2\text{O}$ Doped Into PVDF



with the rate constants k_1 , k_2 , and k_3 shown for the reactions in Scheme 1. The model assumes that gas-phase dioxygen, water, and nitrogen dioxide are in sufficient excess so that the values of k'_1 and k'_2 are essentially constant. In addition, the initial conditions needed to solve of the coupled kinetic equations were that the intermediate and product species (PVDF/Fe(OH)₂ and PVDF/Fe₂O₃) are absent at $t = 0$. The Mössbauer spectra can be used to determine the relative amounts of Fe^{2+} and Fe^{3+} species independently. The peak at $\sim 0.3\text{ mm}\cdot\text{s}^{-1}$ has components from all absorbing species and hence is used as an internal reference. Then, the intensity of the peak at $2.7\text{ mm}\cdot\text{s}^{-1}$ measures the relative amount of Fe^{2+} , and the intensity of the feature at $0.77\text{ mm}\cdot\text{s}^{-1}$ represents the relative amount of Fe^{3+} species, approximated as Fe(OH)_3 and Fe_2O_3 in Scheme 1. The relative intensities of each species are calculated using the eqs S1, S2, and S3 in the Supporting Information and are shown as the solid lines in the insets of Figure 3. At $250\text{ }^{\circ}\text{C}$, the model parameters are $k'_1 = 0.1$, $k'_2 = 0.2$, and $k_3 = 0.01$, and at $300\text{ }^{\circ}\text{C}$, $k'_1 = 7.1$, $k'_2 = 7.2$, and $k_3 = 0.7$. These values are only representative since there are not enough data points to evaluate a unique fit. The model is not ideal but captures the magnitudes of the compositional changes and qualitatively accounts for the increase and then decrease in concentration the intermediate $\text{Fe}[\text{OH}]_2$. The magnitudes of the pseudo-first-order rate constants are consistent with the qualitative observations: the rate constants within the $\text{Fe}^{2+}/\text{Fe}^{3+}$ catalytic cycle are comparable to each other, allowing for cycling, but greater than the rate constant leading to the final decomposition to the oxide product. In addition, the rate constants at the lower temperature are much smaller than those at the higher temperature, as would be

expected by elementary considerations. The limitations of the model arise from two assumptions. First, the concentrations of the gas-phase components (NO_2 , O_2 , and H_2O) are assumed to be constant relative to the concentration of the iron species. Second, the model assumes that at a given temperature, the initial concentrations of Fe(OH)_2 and Fe_2O_3 are zero. However, as the samples are brought to the desired temperature, reaction is occurring during heating. Despite the limitations of the model, however, the general behavior of the reaction is recovered.

Since no Fe^{2+} species are observed in the thermal decomposition of the pure salt, it is apparent that the PVDF environment is critical for the decomposition of NO_2 . Since the thermal reaction occurs above the melting point of any of the PVDF phases, the crystallinity and associated properties are not germane. There may be some weak bonding between the F atoms and the Fe^{3+} ions, but there is no direct evidence of this type of coordination. Finally, the PVDF melt likely retards the transport of the gas-phase products from the nitrate decomposition. Thus, any NO_2 formed that is not at the surface of the melt must diffuse through the viscous polymer allowing an encounter with Fe(OH)_3 sites to activate the reduction of the iron ion.

CONCLUSIONS

$\text{Fe(NO}_3)_3 \cdot 9\text{H}_2\text{O}$ -doped PVDF was studied using IR, XRD, and Mössbauer spectroscopy. At room temperature, the cast films show a high fraction of the ferroelectric β -phase in the crystalline fraction of the polymer host. Moreover, the Mössbauer spectrum shows two Fe^{3+} sites, which are assigned to iron ions located in the β -phase and amorphous regions of the polymer. Heating the films to temperatures below the polymer melting point shows little change in the Mössbauer spectra, but when heated above the polymer melting point, all of the β -phase PVDF is lost and the polymer crystallizes in the α -phase. Further heating leads to decomposition of the iron nitrate dopant. Examination of the Mössbauer spectra of thermal decomposition products of the composite material has identified an unexpected Fe^{2+} intermediate. The initial thermolysis of the nitrate ion gives dioxygen, water, and, presumably, nitrogen dioxide as gas-phase products and the remaining iron as likely in the form of Fe(OH)_3 or FeOOH . The reduction reaction is induced by decomposition of NO_2 into O_2 and N_2 , which is supported by thermodynamic calculations. The Fe^{2+} species, assigned to Fe(OH)_2 , is reoxidized to Fe^{3+} by O_2 so that the final product for the iron species is Fe_2O_3 . A catalytic cycle is proposed showing how the iron sites doped in the polymer promote the loss of NO_2 initially generated by the NO_3^- decomposition. The polymer is a critical component of the catalytic cycle retarding the diffusion of the gas-phase products away from the iron-ion sites. Addition of an external source of NO_2 to determine if the composite material can catalyze the decomposition of this pollutant will be the work of future studies..

ASSOCIATED CONTENT

Supporting Information

The Supporting Information is available free of charge at <https://pubs.acs.org/doi/10.1021/acsomega.2c04970>.

FTIR spectra, Mössbauer spectra, and XRD diffractograms of $\text{Fe(NO}_3)_3 \cdot 9\text{H}_2\text{O}$ heated to various temperatures and kinetic equations ([PDF](#))

AUTHOR INFORMATION

Corresponding Author

William B. Euler – Department of Chemistry, University of Rhode Island, Kingston, Rhode Island 02881, United States;  orcid.org/0000-0002-5317-8510; Email: billeuler@uri.edu

Authors

Lasanthi Sumathirathne – Department of Chemistry, University of Rhode Island, Kingston, Rhode Island 02881, United States

Carson Lawrence Hasselbrink – Department of Chemistry, University of Rhode Island, Kingston, Rhode Island 02881, United States

Dugan Hayes – Department of Chemistry, University of Rhode Island, Kingston, Rhode Island 02881, United States;  orcid.org/0000-0003-4171-5179

Complete contact information is available at:
<https://pubs.acs.org/10.1021/acsomega.2c04970>

Notes

The authors declare no competing financial interest.

ACKNOWLEDGMENTS

This material is based upon work supported by the U.S. Department of Energy, Office of Science, Office of Basic Energy Sciences under award DE-SC0019429, which provided the instrumental resources for the Mössbauer spectroscopy work. The SEM data were acquired at the RI Consortium for Nanoscience and Nanotechnology, a URI College of Engineering core facility partially funded by the National Science Foundation EPSCoR, Cooperative Agreement #OIA-1655221.

REFERENCES

- (1) Kawai, H. The Piezoelectricity of Poly(vinylidene Fluoride). *Japan. J. Appl. Phys.* **1969**, *8*, 975–976.
- (2) Boerio, F. J.; Koenig, J. L. Vibrational Analysis of Poly(vinylidene Fluoride). *J. Polym. Sci. Part A-2* **1971**, *9*, 1517–1523.
- (3) Kobayashi, M.; Tashiro, K.; Tadokoro, H. Molecular Vibrations of Three Crystal Forms of Poly(vinylidene fluoride). *Macromolecules* **1975**, *8*, 158–171.
- (4) Lovinger, A. J. Ferroelectric Polymers. *Science* **1983**, *220*, 1115–1121.
- (5) Vinogradov, A.; Holloway, F. Electro-Mechanical Properties of the Piezoelectric Polymer PVDF. *Ferroelectrics* **1999**, *226*, 169–181.
- (6) Benz, M.; Euler, W. B.; Gregory, O. J. The Role of Solution Phase Water on the Deposition of Thin Films of Poly(vinylidene fluoride). *Macromolecules* **2002**, *35*, 2682–2688.
- (7) Benz, M.; Euler, W. B. Determination of the Crystalline Phases of Poly(vinylidene fluoride) Under Different Preparation Conditions Using Differential Scanning Calorimetry and Infrared Spectroscopy. *J. Appl. Polym. Sci.* **2003**, *89*, 1093–1100.
- (8) Ruan, L.; Yao, X.; Chang, Y.; Zhou, L.; Qin, G.; Zhang, X. Properties and Applications of the β Phase Poly(vinylidene fluoride). *Polymers* **2018**, *10*, 228.
- (9) Liu, J.; Zhao, Q.; Dong, Y.; Sun, X.; Hu, Z.; Dong, H.; Hu, W.; Yan, S. Self-polarized Poly(vinylidene fluoride) Ultrathin Film and Its Piezo/Ferroelectric Properties. *ACS Appl. Mater. Interfaces* **2020**, *12*, 29818–29825.
- (10) Laudari, A.; Barron, J.; Pickett, A.; Guha, S. Tuning Charge Transport in PVDF-Based Organic Ferroelectric Transistors: Status and Outlook. *ACS Appl. Mater. Interfaces* **2020**, *12*, 26757–26775.
- (11) Zhang, Y.; Yang, H.; Dang, Z.; Zhan, S.; Sun, C.; Hu, G.; Lin, Y.; Yuan, Q. Multilayer Structured Poly(vinylidene fluoride)-Based

- Composite Film with Ultrahigh Breakdown Strength and Discharged Energy Density. *ACS Appl. Mater. Interfaces* **2020**, *12*, 22137–22145.
- (12) Huang, Z.-X.; Wang, M.-M.; Feng, Y.-H.; Qu, J.-P. β -Phase Formation of Polyvinylidene Fluoride via Hot Pressing under Cyclic Pulsating Pressure. *Macromolecules* **2020**, *53*, 8494–8501.
- (13) Sahih, M.; Jaramillo-Botero, A.; Goddard, W. A., III; Bedoui, F. Interfacial Interactions in a Model Composite Material: Insights into $\alpha \rightarrow \beta$ Phase Transition of the Magnetite Reinforced Poly(Vinylidene Fluoride) Systems by All-Atom Molecular Dynamics Simulation. *J. Phys. Chem. C* **2021**, *125*, 21635–21644.
- (14) Chu, Z.; Zhao, R.; Wang, B.; Liu, L.; Ma, Z.; Li, Y. Effect of Ions on the Flow-Induced Crystallization of Poly(vinylidene fluoride). *Macromolecules* **2021**, *54*, 3800–3809.
- (15) Luiso, S.; Henry, J. J.; Pourdeyhimi, B.; Fedkiw, P. S. Fabrication and Characterization of Melblown Poly(vinylidene difluoride) Membranes. *ACS Appl. Polym. Mater.* **2020**, *2*, 2849–2857.
- (16) Dhakras, D.; Borkar, V.; Ogale, S.; Jog, J. Enhanced Piezoresponse of Electrospun PVDF Mats with a Touch of Nickel Chloride Hexahydrate Salt. *Nanoscale* **2012**, *4*, 752–756.
- (17) Fontaine, K.; Lopez, W.; Crisman, E.; Derov, J.; Euler, W. B. Doping of PVDF with Cobalt Nitrate: Structural, Electrical, and Magnetic Properties. *J. Polym. Sci. Part A: Polym. Chem.* **2012**, *50*, 3970–3975.
- (18) Reddy, M. O.; Reddy, L. R. M. Structural, Dielectric, Optical, and Magnetic Properties of Ti^{3+} , Cr^{3+} , and Fe^{3+} :PVDF Polymer Films. *J. Polym.* **2013**, *2013*, 1.
- (19) El-Sayed, S.; Abdel-Baset, T. A.; Hassen, A. Dielectric Properties of PVDF Thin Films Doped with 3 wt.% of RCl_3 ($R = Gd$ or Er). *AIP Advances* **2014**, *4*, 037114.
- (20) Tan, K. S.; Gan, W. C.; Velayutham, T. S.; Majid, W. H. Pyroelectricity Enhancement of PVDF Nanocomposite Thin Films Doped with ZnO Nanoparticles. *Smart Mater. Struct.* **2014**, *23*, 125006.
- (21) Amoresi, R. A. C.; Felix, A. A.; Botero, E. R.; Domingues, N. L. C.; Falcão, E. A.; Zaghete, M. A.; Rinaldi, A. W. Crystallinity, Morphology, and High Dielectric Permittivity of NiO Nanosheets Filling Poly(vinylidene fluoride). *Ceram. Internat.* **2015**, *41*, 14733–14739.
- (22) Wu, Z.; Lin, H.; Wang, Y.; Yu, X.; Li, J.; Xiong, Z.; Wang, Y.; Huang, Y.; Chen, T.; Liu, F. Enhanced Catalytic Degradation of 4-NP using a Superhydrophilic PVDF Membrane Decorated with Au Nanoparticles. *RSC Adv.* **2016**, *6*, 62302–62309.
- (23) Zhang, C.; Chi, Q.; Dong, J.; Cui, Y.; Wang, X.; Liu, L.; Lei, Q. Enhanced Dielectric Properties of Poly(vinylidene fluoride) Composites Filled with Nano Iron Oxide-Deposited Barium Titanate Hybrid Particles. *Sci. Reports* **2016**, *6*, 33508.
- (24) Yao, Y.; Lian, C.; Hu, Y.; Zhang, J.; Gao, M.; Zhang, Y.; Wang, S. Heteroatoms Doped Metal Iron-Polyvinylidene Fluoride (PVDF) Membrane for Enhancing Oxidation or Organic Contaminants. *J. Hazard. Mater.* **2017**, *338*, 265–275.
- (25) Correia, D. M.; Costa, C. M.; Lizundia, E.; Sabater i Serra, R.; Gómez-Tejedor, J. A.; Biosca, L. T.; Meseguer-Dueñas, J. M.; Gomez Ribelles, J. L.; Lanceros-Méndez, S. Influence of Cation and Anion Type on the Formation of the Electroactive β -Phase and Thermal and Dynamic Mechanical Properties of Poly(vinylidene fluoride)/Ionic Liquids Blends. *J. Phys. Chem. C* **2019**, *123*, 27917–27926.
- (26) Sutradhar, S.; Saha, S.; Javed, S. Shielding Effectiveness Study of Barium Hexaferrite-Incorporated, β -Phase-Improved Poly(vinylidene fluoride) Composite Film: A Metamaterial Useful for the Reduction of Electromagnetic Pollution. *ACS Appl. Mater. Interfaces* **2019**, *11*, 23701–23713.
- (27) Reyes, A. M.; López Sesenes, R. L.; León Hernández, V. L.; Oubram, O. Effect of Cationic Substitution of Metal Species in Poly(vinylidene difluoride) ($C_2H_2F_2$) by Ab Initio Calculations. *Inorg. Chem.* **2020**, *59*, 15189–15193.
- (28) Chakraborty, T.; Sharma, S.; Ghosh, A.; Mahapatra, A. S.; Chakrabarti, S.; Sutradhar, S. Electromagnetic Shielding Effectiveness of X-Type Hexaferrite- C_3N_4 Binary Nanofiller-Incorporated Poly(vinylidene fluoride) Multiphase Composites. *J. Phys. Chem. C* **2020**, *124*, 19396–19405.
- (29) Jiang, J.; Tu, S.; Fu, R.; Li, J.; Hu, F.; Yan, B.; Gu, Y.; Chen, S. Flexible Piezoelectric Pressure Tactile Sensor Based on Electrospun $BaTiO_3$ /Poly(vinylidene fluoride) Nanocomposite Membrane. *ACS Appl. Mater. Interfaces* **2020**, *12*, 33989–33998.
- (30) Mahdavi, H.; Sajedi, M.; Shahalizade, T.; Heidari, A. A. Preparation and Application of Catalytic Polymeric Membranes Based on PVDF/Cobalt Nanoparticles Supported on MWCNTs. *Polym. Bulletin* **2020**, *77*, 4489–4505.
- (31) Thach, A.; Heiskanen, S.; Lucht, B. L.; Euler, W. B. The Role of Zn^{2+} -Doping on the Surface Chemistry of Poly(vinylidene difluoride) Thin Films. *Surface & Interfaces* **2021**, *23*, 101005.
- (32) Zhang, H. Q.; Euler, W. B. Detection of Gas-Phase Explosive Analytes Using Fluorescent Spectroscopy of Thin Films of Xanthene Dyes. *Sens. Actuat. B: Chem.* **2016**, *225*, 553–562.
- (33) Lin, J.; Malakooti, M. H.; Sodano, H. A. Thermally Stable Poly(vinylidene fluoride) for High-Performance Printable Piezoelectric Devices. *ACS Appl. Mater. Interfaces* **2020**, *12*, 21871–21882.
- (34) Mullen, M.; Euler, W. B. The Influence of Interfacial Effects on the Photophysics of Rhodamine 6G Thin Films on a Poly(vinylidene fluoride) Surface. *Langmuir* **2017**, *33*, 2194–2204.
- (35) Alhasani, M.; Gupta, A.; Euler, W. B. The Influence of Zn^{2+} -doped PVDF on the Fluorescent Properties of Rhodamine 6G. *J. Luminesc.* **2018**, *196*, 116–125.
- (36) Chiang, C.-Y.; Shen, Y. J.; Reddy, M. J.; Chu, P. P. Complexation of Poly(vinylidene fluoride):LiPF₆ Solid Polymer Electrolyte with Enhanced Ion Conduction in ‘Wet’ Form. *J. Power Sources* **2003**, *123*, 222–229.
- (37) Takeda, S.; Saito, Y.; Yagi, T.; Watanabe, K.; Kobayashi, S. Controlling Gel Morphology for Enhancing the Cation Mobility of Poly(vinylidene difluoride)-Based Gel Electrolytes for Lithium Secondary Batteries. *J. Phys. Chem. C* **2020**, *124*, 14082–14088.
- (38) Zhang, W.; Hu, Z.; Fan, C.; Liu, Z.; Han, S.; Liu, J. Construction and Theoretical Calculation of an Ultra-High-Performance LiVPO₄F/C Cathode by B-Doped Pyrolytic Carbon from Poly(vinylidene Fluoride). *ACS Appl. Mater. Interfaces* **2021**, *13*, 15190–15204.
- (39) Biswas, P.; Hoque, N. A.; Thakur, P.; Saikh, M. M.; Roy, S.; Khatun, F.; Bagchi, B.; Das, S. Portable Self-Powered Piezoelectric Nanogenerator and Self-Charging Photo-Power Pack Using In Situ Formed Multifunctional Calcium Phosphate Nanorod-Doped PVDF Films. *Langmuir* **2019**, *35*, 17016–17026.
- (40) Tu, R.; Sprague, E.; Sodano, H. A. Precipitation-Printed High- β Phase Poly(vinylidene fluoride) for Energy Harvesting. *ACS Appl. Mater. Interfaces* **2020**, *12*, 58072–58081.
- (41) Cui, Y.; Feng, Y.; Zhang, T.; Zhang, C.; Chi, Q.; Zhang, Y.; Wang, X.; Chen, Q.; Lei, Q. Excellent Energy Storage Performance of Ferroconcrete-like All-Organic Linear/Ferroelectric Polymer Films Utilizing Interface Engineering. *ACS Appl. Mater. Interfaces* **2020**, *12*, S6424–S6434.
- (42) Kong, T.-H.; Lee, S.-S.; Choi, G.-J.; Park, I.-K. Churros-like Polyvinylidene Fluoride Nanofibers for Enhancing Output Performance of Triboelectric Nanogenerators. *ACS Appl. Mater. Interfaces* **2020**, *12*, 17824–17832.
- (43) Yang, L.; Zhao, Q.; Chen, K.; Ma, Y.; Wu, Y.; Ji, H.; Qiu, J. PVDF-Based Composition-Gradient Multilayered Nanocomposites for Flexible High-Performance Piezoelectric Nanogenerators. *ACS Appl. Mater. Interfaces* **2020**, *12*, 11045–11054.
- (44) Kise, H.; Ogata, H. Phase Transfer Catalysis in Dehydrofluorination of Poly(vinylidene Fluoride) by Aqueous Sodium Hydroxide Solutions. *J. Polym. Sci.: Polym. Chem. Ed.* **1983**, *21*, 3443–3451.
- (45) Chen, Y.; Liu, L.; Wang, Y.; Kim, H. Preparation of Porous PVDF-NiB Capsules as Catalytic Adsorbents for Hydrogen Generation from Sodium Borohydride. *Fuel Processing Tech* **2011**, *92*, 1368–1373.
- (46) Wang, W.; Chen, X.; Zhao, C.; Zhao, B.; Dong, H.; Ma, S.; Li, L.; Chen, L.; Zhang, B. Cross-Flow Catalysis Behavior of a PVDF/

- SiO₂@Ag Nanoparticles Composite Membrane. *Polymers* **2018**, *10*, 59.
- (47) Lyubimenko, R.; Busko, D.; Richards, B. S.; Schäfer, A. I.; Turshatov, A. Efficient Photocatalytic Removal of Methylene Blue Using a Metalloporphyrin-Poly(vinylidene fluoride) Hybrid Membrane in a Flow-Through Reactor. *ACS Appl. Mater. Interfaces* **2019**, *11*, 31763–31776.
- (48) Sumathirathne, L.; Euler, W. B. Catalysis of the Thermal Decomposition of Transition Metal Nitrate Hydrates by Poly(vinylidene difluoride). *Polymers* **2021**, *13*, 3112.
- (49) Fu, C.; Zhu, H.; Hoshino, N.; Akutagawa, T.; Mitsuishi, M. Interfacial Nanostructuring of Poly(vinylidene fluoride) Homopolymer with Predominant Ferroelectric Phase. *Langmuir* **2020**, *36*, 14083–14091.
- (50) Mishra, S.; Sahoo, R.; Unnikrishnan, L.; Ramadoss, A.; Mohanty, S.; Nayak, S. K. Effect of Multi-Step Processing on the Structural, Morphological and Dielectric Behaviour of PVDF Films. *Ionics* **2020**, *26*, 6069–6081.
- (51) He, Z.; Mahmud, S.; Zhao, S.; Yang, Y.; Zhu, L.; Zhao, Y.; Zeng, Q.; Xiong, Z. C.; Hu, C. Hierarchically Active Poly(vinylidene fluoride) Membrane Fabricated by In Situ Generated Zero-Valent Iron for Fouling Reduction. *ACS Appl. Mater. Interfaces* **2020**, *12*, 10993–11004.
- (52) Winter, E. R. S. The Catalytic Decomposition of Nitric Oxide by Metallic Oxides. *J. Catal.* **1971**, *22*, 158–170.
- (53) Shimokawabe, M.; Ohi, A.; Takezawa, N. Catalytic Decomposition of Nitrogen Dioxide over Various Metal Oxides. *Appl. Catal. A: General* **1992**, *85*, 129–133.
- (54) Damma, D.; Boningari, T.; Ettireddy, P. R.; Reddy, B. M.; Smirniotis, P. G. Direct Decomposition of NO_x over TiO₂ Supported Transition Metal Oxides at Low Temperatures. *Ind. Eng. Chem. Res.* **2018**, *57*, 16615–16621.
- (55) Yokomichi, Y.; Nakayama, T.; Okada, O.; Yokoi, Y.; Takahashi, I.; Uchida, H.; Ishikawa, H.; Yamaguchi, R.; Matsui, H.; Yamabe, T. Fundamental Study on the NO_x Direct Decomposition Catalysts. *Catalys. Today* **1996**, *29*, 155–160.
- (56) Garin, F. Mechanism of NO_x Decomposition. *Appl. Catalys. A: General* **2001**, *222*, 183–219.
- (57) Roy, S.; Hegde, M. S.; Madras, G. Catalysis for NO_x Abatement. *Appl. Energy* **2009**, *86*, 2283–2297.
- (58) Imanaka, N.; Masui, T. Advances in Direct NO_x Decomposition Catalysts. *Appl. Catalys. A: General* **2012**, *431*–432, 1–8.
- (59) Huang, X.; Ding, J.; Zhong, Q. Catalytic Decomposition of H₂O₂ over Fe-Based Catalysts for Simultaneous Removal of NO_x and SO₂. *Appl. Sur. Sci.* **2015**, *326*, 66–72.
- (60) Roberts, C. A.; Paidi, V. K.; Shepit, M.; Peck, T. C.; Stamm Masias, K. L. S.; van Lierop, J.; Reddy, G. K. Effect of Cu Substitution on the Structure and Reactivity of Cu_xCo_{3-x}O₄ Spinel Catalysts for Direct NO_x Decomposition. *Catalys. Today* **2021**, *360*, 204–212.
- (61) Addison, C. C.; Harrison, P. G.; Logan, N.; Blackwell, L.; Jones, D. H. Mössbauer Study of the Thermal Decomposition of Dinitrogen Tetroxide Solvates of Iron(III) Nitrate. *J. Chem. Soc. Dalton Trans.* **1975**, 830833.
- (62) Prescher, C.; McCammon, C.; Dubrovinsky, L. M.A. A Program for Analyzing Energy-Domain Mössbauer Spectra From Conventional and Synchrotron Sources. *J. Appl. Cryst.* **2012**, *45*, 329–331.
- (63) Martins, P.; Lopes, A. C.; Lanceros-Mendez, S. Electroactive Phases of Poly(Vinylidene Fluoride): Determination, Processing and Applications. *Progr. Polym. Sci.* **2014**, *39*, 683–706.
- (64) Cao, X.; Prozorov, R.; Koltypin, Yu.; Kataby, G.; Felner, I.; Gedanken, A. Synthesis of Pure Amorphous Fe₂O₃. *J. Mater. Res.* **1997**, *12*, 402–406.
- (65) Kuzmann, E.; Nagy, S.; Vérites, A. Critical Review of Analytical Applications of Mössbauer Spectroscopy Illustrated by Mineralogical and Geological Examples (IUPAC Technical Report). *Pure Appl. Chem.* **2003**, *75*, 801–858.
- (66) Baldokhin, Yu. V.; Suzdalev, I. P.; Prusakov, V. E.; Burnazyan, D. A.; Korneev, V. P.; Kovalenko, L. V.; Folmanis, G. E. A Study of Nanostructures Formed in the Hydrogen Reduction of Fe(OH)₃. *Russ. J. Phys. Chem. B* **2012**, *6*, 81–88.
- (67) Au-Yeung, S. C. F.; Denes, G.; Greeden, J. E.; Eaton, D. R.; Birchall, T. A Novel Route to “Iron Trihydroxide, Fe(OH)₃: Characterization and Magnetic Properties. *Inorg. Chem.* **1984**, *23*, 1513–1517.
- (68) <https://webbook.nist.gov/chemistry/>. accessed May 11, 2021.

□ Recommended by ACS

Mechanisms of Sonochemical Transformation of Nitrate and Nitrite under Different Conditions: Influence of Additives and pH

Nina Hoinkis and Marta I. Litter

OCTOBER 25, 2022

INDUSTRIAL & ENGINEERING CHEMISTRY RESEARCH

READ ▶

One-Step Synthesis of Ammonia Directly from Wet Air/N₂ by Plasma Combined with a γ-Al₂O₃ Catalyst

Jiayu Feng, Maohong Fan, et al.

JANUARY 06, 2023

ACS SUSTAINABLE CHEMISTRY & ENGINEERING

READ ▶

Ozone- and Hydroxyl Radical-Mediated Oxidation of Pharmaceutical Compounds Using Ni-Doped Sb-SnO₂ Anodes: Degradation Kinetics and Transformation Products

Yi Zhang, Michael R. Hoffmann, et al.

JANUARY 26, 2023

ACS ES&T ENGINEERING

READ ▶

Space Charge Contributions to the Dielectric Response and Breakdown Strength of High-Temperature Poly(ether imide)/Polyimide Blends

Vida Jurečić, Vid Bobnar, et al.

JANUARY 13, 2023

MACROMOLECULES

READ ▶

Get More Suggestions >